Investigating Nickel Ferrite (NiFe₂O₄) Nanoparticles for Magnetic Hyperthermia Applications

Muhammad Naqeeb Ahmad[1], Hamid Khan[1], Lubna Islam[2], M. Hisham Alnasir[3], Shahid Nisar Ahmad[4], Muhammad Tauseef Qureshi[5*], Muhamamd Yaqoob Khan[1*]

[1] Department of Physics, Kohat University of Science and Technology, 26000 Kohat, Khyber Pakhtunkhwa, Pakistan
[2] Department of Pharmacy, University of Malakand, Chakdara, Dir (lower), Khyber Pakhtunkhwa, Pakistan
[3] Department of Applied Physics, Federal Urdu University of Arts, Science and Technology, Islamabad, Pakistan
[4] National Center for Physics,Shahdara Valley Road,45320 Islamabad, Pakistan
[5] Department of Basic Sciences, College of Preparatory Year, University of Hail, Hail, Saudi Arabia

ARTICLE INFO

ABSTRACT

Many new promising therapeutic and diagnostic methods in medical science use magnetic nanoparticles (MNPs). Drug targeting, tumor detection, and magnetic hyperthermia treatment are the most common fields of interest where already clinical trials are being performed. Nickel ferrite (NiFe₂O₄) nanoparticles have received much attention for their potential applications in such fields. A series of samples of Nickel ferrite (NiFe₂O₄) nanoparticles have been synthesized using a co-precipitation route at different annealing temperatures ranging from 150 ℃ to 1000 ℃ and labeling them as S1, S2, S3, S4, and S5. The average particle size obtained from XRD data is found to lie in the range of 15 – 55 nm. The crystal structure of the prepared NiFe₂O₄ four samples annealed at different temperatures is FCC with a lattice constant of 8.34 Å, which agrees with the values. The magnetic properties of the samples were investigated from temperature-dependent hysteresis loops using Vibrating Sample Magnetometer (VSM). The saturation magnetization (coercivity) is found to increase (decrease) with particle size. The hyperthermia measurements are performed by applying alternating magnetic fields of various amplitudes (Oe) and frequencies (kHz). The measured heating ability of the prepared nanoparticles is obtained from the so-called specific absorption rate (SAR), which is found to increase with increasing frequency and field amplitudes. Using the experimentally obtained SAR value, we also used MATLAB code to model the heat diffusion equation to get information on the temperature rise within the tumor as a function of tumor radius and treatment time.The sample S4 annealed at a temperature of 900 ℃ is found to be the most suitable candidate for hyperthermia applications at the frequency of 543 kHz because of its capability to produce heat in the therapeutic range of 42-48 ℃ and with *an SAR* value of 500 W/g.

*Corresponding Authors' Email: yaqoob@kust.edu.pk, m.qureshi@uoh.edu.sa

1.   Introduction

Cancer is the leading cause of death worldwide. Surgery, radiation therapy, and chemotherapyare the most commonly used procedures to treat cancer. However, the efficacy of these procedures is limited, and each one has its side effects(Hussain et al., 2021).

Hippocrates proposed hyperthermia or thermotherapy and stated that all skin tumors on the outer surface of the body may be treated with hot iron (Tomitaka & Takemura, 2019). Hyperthermia was used for the first time, and a Swedish gynecologist Westermarck used hyperthermia in 1898to treat cervical cancer by running hot water through an intracavity spiral tube (Westermark, 1898). Hyperthermia is acknowledged as a distinct therapy used alone or as an adjuvant to chemotherapy or radiotherapy (Bañobre-López, Teijeiro, & Rivas, 2013; Kumar & Mohammad, 2011). The biochemical processes occurring in the cell, such as metastasis, are vulnerable to alteration in temperature. A few centigrade temperature rises in body temperature, i.e., from 37 ℃ - (42 to 48) ℃, is required to kill the cancer cell (Dennis et al., 2008).

Furthermore, the temperature range 42 ℃ - 48 ℃ can either be used as an adjuvant therapy or can directly kill the cancer cells by a process called thermoabalation, a function of time and temperature (Hildebrandt et al., 2002). Tumor cells have poor heat dissipation and constrained blood flow due to their abnormal growth and disorganized atomic structure. Therefore, cancerous cells are highly sensitive to temperature than healthy cells (Cihoric et al., 2015; Kakehi et al., 1990; Kuwano et al., 1995). In combination with radiotherapy and chemotherapy, hyperthermia has shown 39% to 85% of complete response rate (Kuwano et al., 1995). However, hyperthermia has side effects, such as temperature control within the tumor and non-localized heating, thereby damaging the healthy cells. Moreover, secondary harmful effects have been found with normal tissues when hyperthermia was combined with other treatment modalities (Bañobre-López et al., 2013).

To overcome the problems associated with hyperthermia, an alternative approach, known as magnetic hyperthermia, was used to treat cancer. Magnetic hyperthermia has been found to be a promising technique for treating cancerusing magnetic nanoparticles(Singh, 1990; Szasz, Szigeti, Szasz, & Benyo, 2018).When magnetic nanoparticles are subjected to RF fields, heat is generated through various loss mechanisms, such as hysteresis and relaxationallosses. Hysteresis losses occur in multidomain particles, whereas relaxation losses occur in single-domain superparamagneticnanoparticles (SPMNPs). Ideally, the nanoparticles used for magnetic hyperthermia should be superparamagnetic. When SPMNPs are exposed to radiofrequency fields, their magnetic moments rotate in the direction of the field and then relax back to the original field orientation called Néel relaxation. Brownian relaxation is due to the rotation of the particle within a viscous fluid where heat is produced due to friction at the surface particles(Kalambur, Han, Hammer, Shield, & Bischof, 2005).

Superparamagnetic or ferromagnetic nanoparticles, i.e., Fe_3O_4 /$_\gamma$ - Fe_2O_3, have been extensively investigatedin magnetichyperthermia to treat cancer. Recent challenges in magnetic hyperthermia are high heat efficiency and controlled in vivo temperature in the therapeutic limit of 42 – 48 °C(Pradhan, Giri, Banerjee, Bellare, & Bahadur, 2007). The heating efficiency of probed nanoparticles is determined by measuring the specific absorption rate (SAR) as given by equation (1).

$$SAR = C.\left(\frac{dT}{dt}\right)_{t=0}.\frac{m_{sample}}{m_{mag.}} \tag{1}$$

where m is the mass of the sample, C is the specific heat capacity of the sample, and m_{mag} is the mass fraction of the magnetic component. The value of SAR determines the dose of the nanoparticles; the higher the SAR value, the low dose will be required to treat cancer, thereby reducing the side effects.

Nickel ferrite ($NiFe_2O_4$) is a soft spinel ferrite (Šepelák et al., 2007). Nickel ferrite ($NiFe_2O_4$) has been found to be the alternative to Fe_3O_4 /$_\gamma$ - Fe_2O_3 due to its biocompatibility and heating efficiency (Bae, Lee, & Takemura, 2006; Menelaou, Georgoula, Simeonidis, & Dendrinou-Samara, 2014; Stefanou et al., 2014). In this work, we have synthesized nickel ferrite ($NiFe_2O_4$) from nickel and iron nitrate salts using the chemical co-precipitation route. The prepared samples were further calcined/annealed at different temperatures to vary the particle size and crystallinity. The structural, magnetic, and hyperthermia measurements were carried out to find the suitability of Nickel ferrite ($NiFe_2O_4$) for magnetic hyperthermia applications.

2. Experimental Details

The $NiFe_2O_4$ sample was prepared using a chemical co–precipitation route. The details of the synthesis procedureare given in the work carried out to synthesize tin oxide nanoparticlesby Tazikeh, S. *et al.*(Tazikeh, Akbari, Talebi, & Talebi, 2014).The chemical precursors used for the synthesis of $NiFe_2O_4$ were nickel nitrate hexahydrate (Ni $(NO_2)_3.6H_2O$) and iron nitrate nonahydrate (Fe $(NO_3)_3.9H_2O$). The aqueous solution was prepared by mixingiron nitrate and nickel nitrate in the de-ionized water. Thensodium hydroxide (NaOH) was added slowlywhile continuously stirring to set the pH value at 10–11. The solution was heatedat 100 ºC for one hour and then washed with ethanol to remove excess sodium and nitrate traces. The precipitates formed were left to dry at 50 ºC overnight. The obtained sample was labeledS1. The resultant sample was ground and calcined at various temperatures, i.e., 600 ºC, 800 ºC, 900 ºC, and 1000 ºC each for ten hours and was labeled as S2, S3, S4, and S5, respectively.

XRD wasused to obtain structural parameters such as crystallite size and lattice parameters.A scanning electron microscope (SEM)with a magnification power of up to 1,000,000 X and a resolving power of 10 Åwas used to study the surface morphology of the samples. Magnetic properties in the temperature range of 100 K to 300 Kwere carried out by Vibrating Sample Magnetometer (VSM). The heating efficiency was investigated by using an RF-induction unit.Finally, a simple model based on a heat diffusion equation is used (in MATLAB) to see the temperature rise as a function of the time of treatment and tumor radius.

3. Results and Discussion
3.1. Structural Characterization
3.1.1.XRD Analysis

The phase identification of the product was carried out by powder X-ray diffraction (XRD, Bruker D8-advance, Germany). The XRD patterns were collected by steps of 0.02 in the 20 – 80 degree range with a constant counting time of 0.6 s per step at room temperature. The phase formation and purity were examined by powder x-ray diffraction using Cu-Ka (λ = 1.5425 Å) radiation. The XRD graph explains features of synthesized nanoparticles of $NiFe_2O_4$, especially the effect of annealing on phase contribution and change/increase in crystallize size.
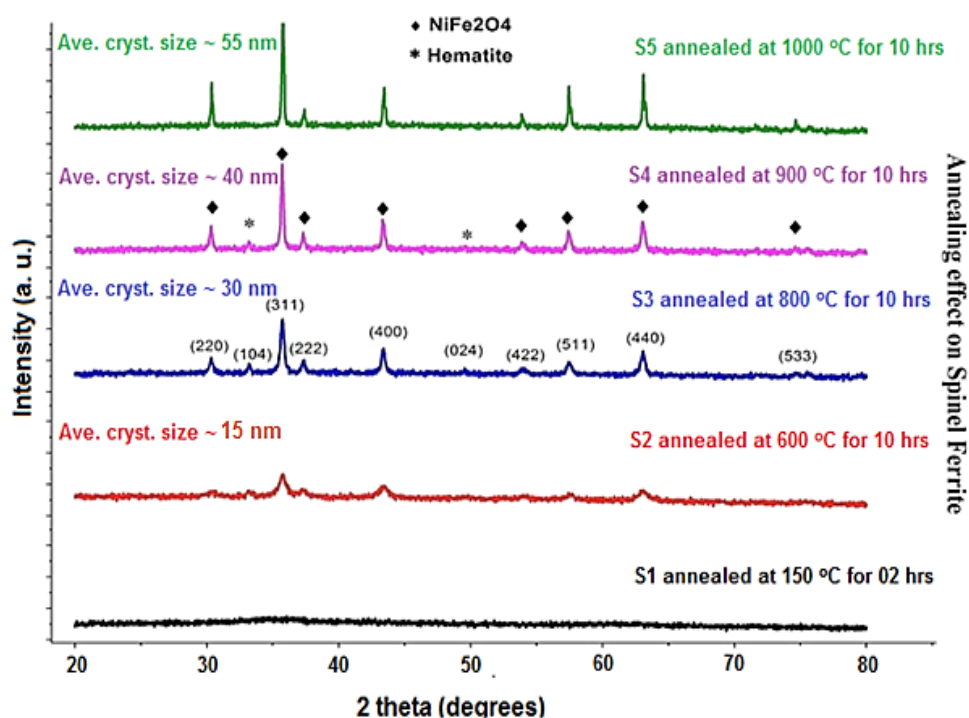

Figure 1: XRD intensity as a function of diffracted angle for different samples of $NiFe_2O_4$ nanoparticles annealed at different temperatures

The XRD pattern of the prepared nanoparticles of $NiFe_2O_4$ is shown in Fig. 1. Almost a similar data trend can be seen in these figures as reported in the literature. Seven major peaks can be observed, which correspond to the crystal planes (220), (311), (222), (400), (422), (511), and (440) with the Face Centered Cubic (FCC) spinel structure of $NiFe_2O_4$ with Fe cations at tetrahedral sites and nickel cations at octahedral sites. Bragg's reflections are found to be sharp and intense and have been indexed, confirming the formation of cubic spinel structure in a single phase.

The average crystal size is determined by the Debye-Scherrer equation

$$t = \frac{K\lambda}{\beta cos\theta}$$
(2)

Where λ is the X-ray wavelength (Cu K_α radiation and equals to 0.154 nm), θ is the Bragg diffraction angle (in radians), and β is the FWHM (full-width half maximum) or integral breadth of the XRD peak appearing at the diffraction angles θ. *t* is the thickness of crystallite, and *K* is constant dependent on the crystalline shape. The crystalline size is found at the maximum intensity peak of the plane (311) to be 15, 30, 40, and 55 nm for S2, S3, S4, and S5 samples annealed at different temperatures, respectively. Annealed samples have more intensepeaks than prepared ones. It indicates more crystallinity of the nickel ferrite. The effect of increasing temperature on the improvement of the crystallinity of nickel ferrite and the conversion of some nickel and iron oxides to produce nickel ferrite crystallites can be seen in the same figure. The crystallization of nickel ferrite improves at increasing the annealing temperature.

All the reflections are indexed based on the standard index system. The broad peaks of the XRD patterns stipulate that the particles of the synthesized samples are in the nanometer range. The presence of hematite diffraction peaks contributes as an impurity and reveals the formation of a multi-phase. S5 does not show the presence of a hematite phase. Still, the Diffused Reflectance Spectra (DRS) show an extra line of band gap energy (as shown below in Fig.6). It may be due to the effects of fluoresces, and the phase contribution of hematite is thus ignorable. All four samples' calculated cubic lattice parameters are the same (8.34 Å)as thatfor the standard $NiFe_2O_4$ (8.34 Å). Structural parameters are given in Table 1.

Table 1
Lattice constants and average crystallite size obtained from XRD data for different samples of $NiFe_2O_4$

Structural Parameter	S2	S3	S4	S5
Lattice constant (a=b=c) (Å)	8.332	8.334	8.342	8.343
The average crystallite size (nm)	15	30	40	55

3.1.2.SEM Analysis

The Scanning Electron Microscope (SEM) images of samples S3, S4, and S5 are shown in Fig. 2. The images depict mass agglomerations of tiny particles resulting in large particles. he images show dense aggregation because of high surface energies and tend to grow into larger accumulation.

3.2. Magnetic Measurements

The magnetic behavior of $NiFe_2O_4$ nanoparticles was investigated using Vibrating Sample Magnetometry (VSM) (Lakeshore VSM 7410) with an applied field of 10 kOe or 1 Tesla.The magnetic measurements, i.e.,magnetization as a function of the fieldfor the two samples S4, S5 taken attemperatures in the range of 150 K to 300 K, are shown in Fig. 3. The hysteresis loops of the samples S4 and S5 at 300 K have been compared in Fig. 3 (a).
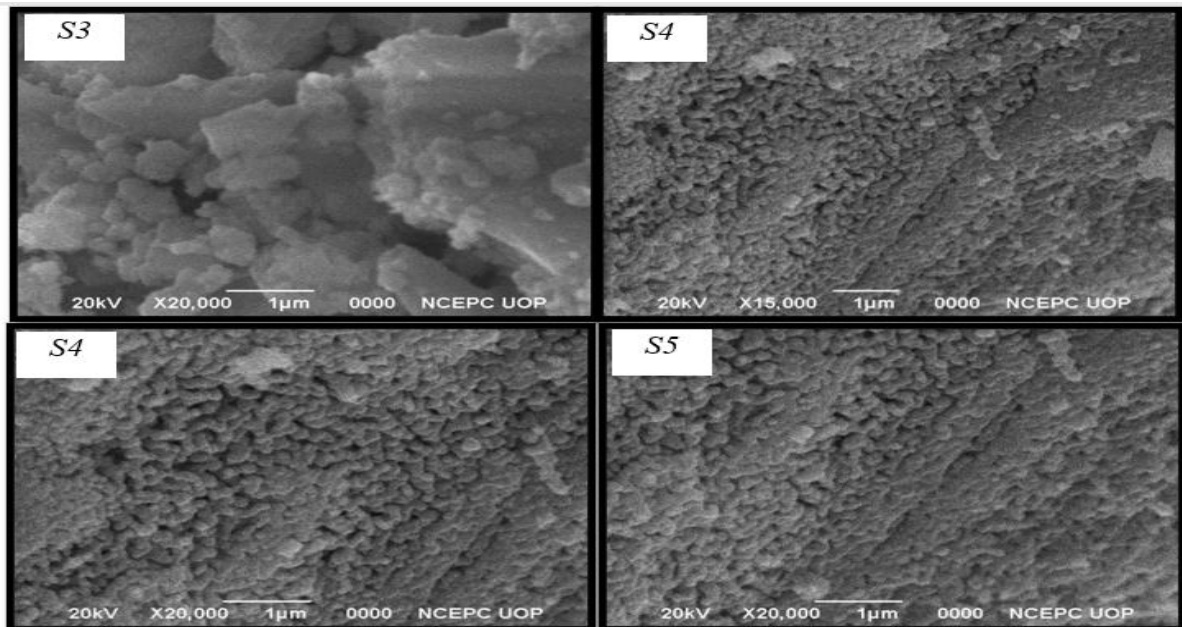
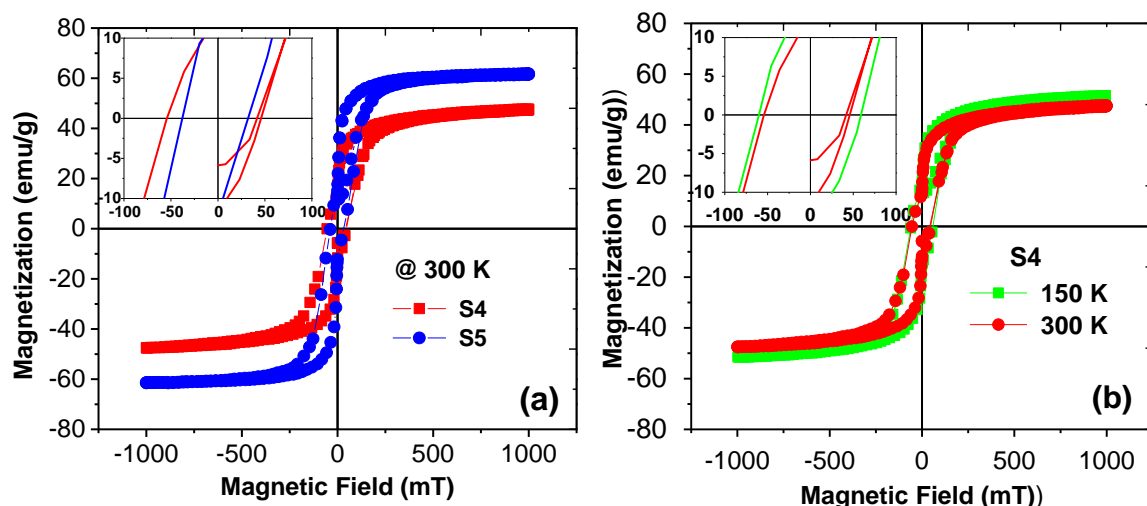**Figure 2: The SEM images of samples S3, S4, and S5**

Figure 3: Magnetic hysteresis loopsfor (a) S4 and S5 at 300 Kand (b) S4 at two different temperatures, i.e., 150 K and 300 K

The magnetic properties of the materials, such as magnetization and coercivity, strongly depend on the particle size, shape, crystallinity, etc.The samples show ferromagnetic behavior. The temperature and the size of the MNPs significantly influence the magnetic properties, as depicted in Fig. 3 and Table 2.It can be observed from Fig. 3(a) that S5 has a larger magnetization than S4 because magnetization increases with increasing particle size. The samples' saturation magnetization (M_s) as a function of temperature is plotted in Fig. 4. It can be seen that M_s decreases with the rise in temperature for both samples. This can be attributed to the thermal effects dominating at high temperatures. However, sample S5 due to its large particle size has relatively large magnetization at all temperatures compared to sample S4. The magnetic parameters determined from these plots have been listed in table 2.

Table 2
Crystallite size, saturation magnetization, coercivity, and retentivity of NiFe2O4 at 300 K

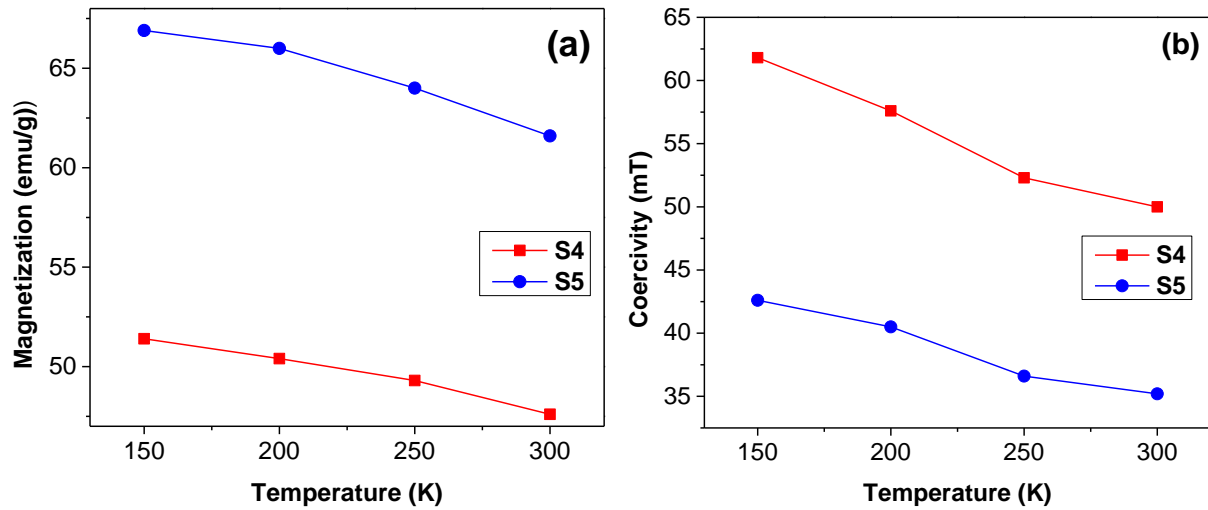| Sample	Calcination temperature T (ºC)	Crystallite Size D (nm)	Saturation magnetization M_s (emu/g)	Coercivity H_c (mT)	Retentivity M_r (emu/g)
S4	900	40	47.62	50.01	13.55
S5	1000	55	61.65	35.17	20.22

Figure 4: (a) Magnetizationand (b) coercivity as a function of temperature for two samples, S4 and S5, annealed at 900 ºC and 1000 ºC, respectively

The inset of Fig. 3(a) shows the coercivity of the samples. The coercivity of S4 is larger than S5, likely due to the transition of the particle size from single domain to multidomainas the particle size increases. However, the product of coercivity and magnetization (Zeeman energy) for S4 is comparable to that of S5, suggesting that sample S4 might have the same heating ability as sample S5. This is because the heating ability of the sample in an RF field depends upon both the magnetization and coercivity(anisotropy).

Table 3
The coercivity of samples at different temperatures

Sample	Coercivity (mT)			
	150 K	200 K	250 K	300 K
S3 (50 mg)	43.31	39.97	38.94	33.85
S4 (30 mg)	61.85	57.62	52.29	50.01
S5 (50 mg)	42.65	40.46	36.64	35.17

The coercivitiesofthe samples S4 and S5 from their *M(H)* loops taken at various temperatures have been plottedin Fig. 5. The decrease in coercivity can be observed with increasing temperature. The decrease in coercivity may be due to the effects of thermal fluctuations of the blocked moment across the anisotropy barrier. Coercivity is strongly dependent on particle size as well. If we correlate coercivity with particle size, it can be inferred that it (coercivity) directly relates to particle size - it decreases as the size of particles increases. Further, the coercivity of S4 is greater than that of S3 and S5 due to the small mass(30 mg) of S4 than that of S3 and S5 (50 mg).Coercivity values as a function of temperature are given in Table 3 below.

3.3. Hyperthermia Measurements

Magnetically induced heating measurements were carried out on 50 mg powder for the samples S4 and S5 under an alternating field strength and frequency of230 Ôeand 543 kHz, 200 Ôe, and 172 kHz, respectively. The results are shown in Fig. 5. It can be seen that heating is produced in both the samples at the applied fields and frequencies. The heating produced by magnetic nanoparticles depends on parameters such as particle size, saturation magnetization, effective anisotropy, applied field strength, and frequency. The effect of field strength and frequency can be observedin Fig. 5.

The rapid increase in temperature can be observed (Fig. 5(a) compared to Fig. 5(b)) with the increase in frequency. Sample S5 has a large heating potential compared to sample S4 due to its relatively large saturation magnetization. The heating produced is usually quantified by measuring the specific absorption rate (SAR), the power released per unit mass by MNPs in heat. Maximizing the SAR is an essential objective in magnetothermal therapy in order to reduce the dosage of the magnetic nanoparticles.
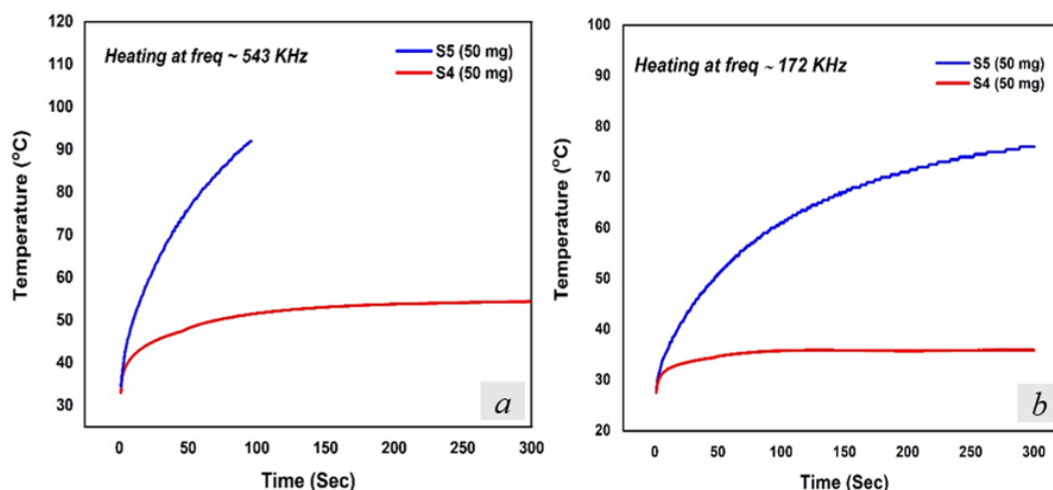
Figure 5: (a, b) Heating Efficiency of S4 & S5 samples at 543 kHz and 172 kHz at external fields 23mT and 20mT, respectively

We measured the specific absorption rate (*SAR*) using equation (2). The initial slope values $\left(\frac{dT}{dt}\right)_{t=0}$ were extracted from their heating curves in Fig. 5.The obtained SAR values are listed in Table 4.Thevalues of SAR obtained are 500 W/g and 450 W/g at 543 kHz for the samples S5 and S4, respectively.In addition, it can also be seen that sample S4 produces heat in the therapeutic range of 42 – 48 ℃ at 543 kHz since the cancer cells are more sensitive to this temperature range as compared to the healthy cells. Hence, sample S4 is found to be most suitable at the given frequency of 543 kHz for magnetic hyperthermia application.

Table 4
Specific Absorption Rate (SAR) of S4 & S5 comparison of S5 at two fields and frequencies

Samples	SAR (W/g)	
	230 Oe	200 Oe
	172 kHz	543 kHz
S4	400	450
S5	480	500

3.4. DRS Analysis

Diffuse Reflectance Spectroscopy (DRS) technique was used to study band gaps from the light absorption spectrum. The band gap of $NiFe_2O_4$ nanoparticles was determined by using Tauc, Davis, and Mott relation given by:

$$(hv\alpha)^{\frac{1}{n}} = A\left(hv - E_g\right) \tag{3}$$

Where α is the absorption coefficient, $v$is the light frequency,$and\ A$ is a proportionality constant,$E_g$is the band gap energy. Band gap energy can determine from the plot$(hv\alpha)^{1/n}$as a function of energy (hv), as shown in Fig. 6, by extrapolating the straight line to the axis intercept.

There are two values of the energy gap, as evident from Fig. 6 for S2 – S5. The second band gap is due to the presence of hematite. The presence of the hematite phase is already confirmed from XRD data. The sample S6 is not annealed separately from other samples - it is collected after TGA/DTA analysis which is made at 1200℃. In this sample, no other band gap energy line can be seen as only $NiFe_2O_4$ is present, and the hematite phase is absent. The value of the indirect band gap of energy for $NiFe_2O_4$ is found to be around 1.53 eV, and for hematite, it is in the range of 1.82 - 1.96 eV.
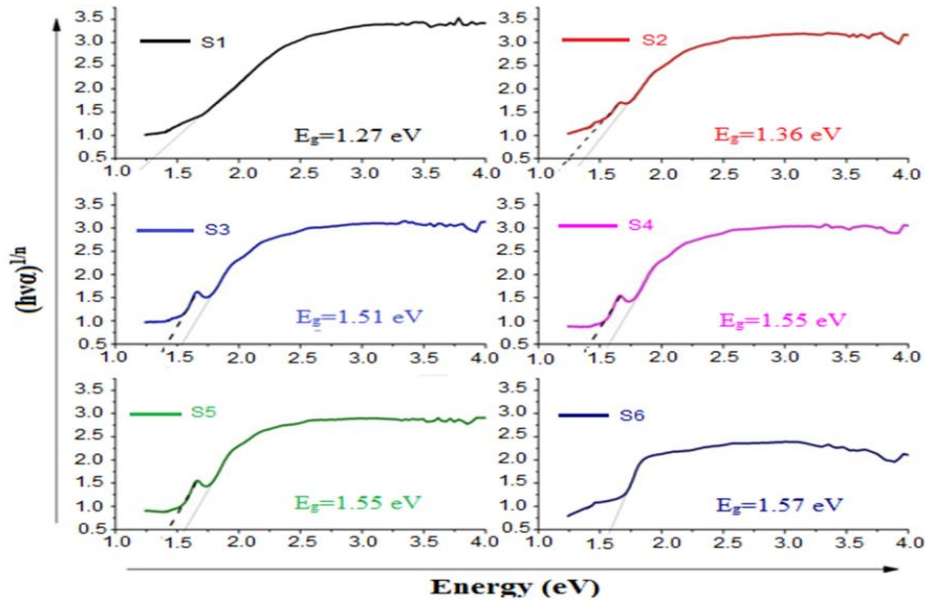
Figure 6: Extraction of energy gap value for NiFe$_2$O$_4$ from the Tauc-plot for different samples (S1 - S6) annealed at 150 ºC (S1), 600 ºC (S2), 800 ºC (S3), 900 ºC (S4), 1000 ºC (S5) and at 1200 ºC (S6) each for ten hours

3.5. Thermal analysis

Thermal studies of nanoparticles include the determination of their decomposition and crystallization temperature. For this, thermogravimetric and differential thermal analysis (TG-DTA) techniques were used in which dried precursors of NiFe$_2$O$_4$ were obtained via the co-precipitation method using a thermal analyzer (Mettler Toledo star system). The TG-DTA curve in Fig. 7 shows that major weight loss occurs from 270 ºC to 420 ºC. The plateau formed from 450 ºC to 1200 ºC indicates the formation of NiFe$_2$O$_4$ crystallites already confirmed by XRD.
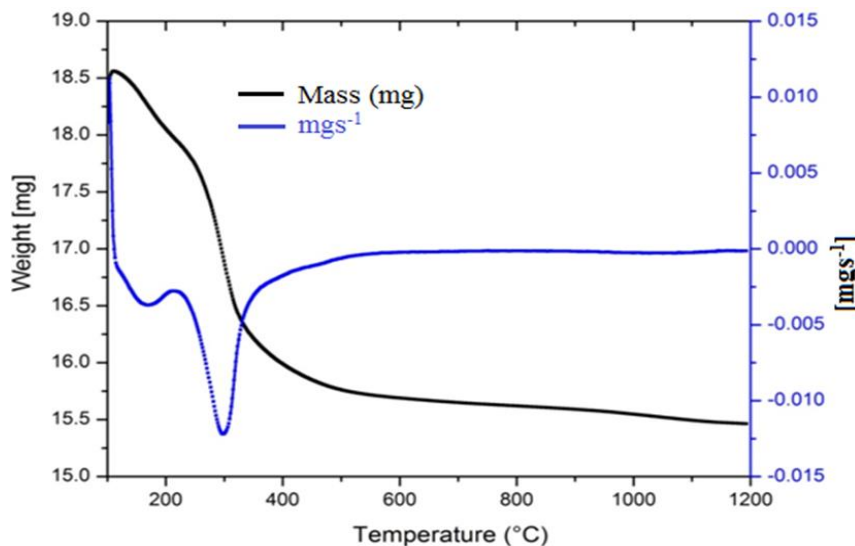

Figure 7: TGA/DTA curve of NiFe$_2$O$_4$ nanoparticles dried at 100 ºC

3.6. Modeling Approach and Mathematical Modelling

An analytical approach was adopted to meet the heat propagation problem produced by magnetic nanoparticles (NiFe$_2$O$_4$) within. The thermal properties of human lung tissue obtained from literature were used,and the value of heat produced by the MNPs was used from our experimental data.

Assumptions

Some assumptions in our model, such as the spherical shape of the tumor and linear decrease in particle concentration from the center to the periphery of the tumor, are made. This linear particle concentration correlation is also applied to power density. According to the assumed initial conditions, the temperature of the tumor and healthy tissues, as well as that of the boundary/interface between healthy and tumorous tissue (r = R), is assumed to be the same - nearly equal to body temperature (T_0= 37 ℃).

The heat diffusion equation is used to model thedistribution of heat behavior governed by the MNPs due to the application of alternating magnetic field and is given by:

$$\rho c \frac{\partial T}{\partial t} = \kappa \frac{1}{r^2} \frac{\partial}{\partial r} \left(r^2 \frac{\partial T}{\partial r} \right) + wr \tag{4}$$

Where T(r, t) is the temperature at a discrete point in the tissue, which continuously varies with time; $wr = P$ is the power density, $\kappa$is the thermal conductivity; c is the specific heat capacity, and ρ is the density of a lung's tumor. The boundary conditions are given by:

$T(0,0) = T_0$ at equilibrium temperature at the origin/center of the tumor,
$T(r,0) = T_0$ at the interface between the tumor and surroundings
$T(r,t) = T$ at any arbitrary value of r and t.

For simplification to solve the equation, we transform T into a new variable Φ, i.e.,

$$\Phi(r,t) = r\Delta T \text{where} \Delta T = T(r,t) - T_0 \tag{5}$$

Differentiating this concerning 't';

$$\frac{1}{r} \frac{\partial \Phi(r,t)}{\partial t} = \frac{\partial T(r,t)}{\partial t} \tag{6}$$

And concerning 'r';

$$r \frac{\partial^2 \Phi(r,t)}{\partial r^2} = \frac{\partial}{\partial r} \left(r^2 \frac{\partial T(r,t)}{\partial r} \right) \tag{7}$$

Now substituting equationseqs. (6) & (7) into eq. (1) we arrive at:

$$\frac{1}{D} \frac{\partial \Phi}{\partial t} = \frac{\partial^2 \Phi(r,t)}{\partial r^2} + \frac{w}{\kappa} r^2 \tag{8}$$

Where $D = \frac{\kappa}{cp}$is the thermal diffusivity of the tumor. The boundary conditions also need to be transformed in terms of Φ.At $r = 0$, by assuming the finiteness of temperature at the interface:

$\Phi(0,t) = r\,(T(0,t) - T_0) = 0$
$\Phi(R,t) = R(T(R,t) - T_0) = 0$
$\Phi(r,0) = r(T(r,0) - T_0) = 0$
$\Phi(r,t) = r(T(r,t) - T_0) = 0$

Due to the homogeneity of boundary conditions, the source term allows us to break the solution to the equation into the homogenous and steady-state equation.
By putting t = 0, the solution to steady state equation (8) becomes:

$$\Phi_s = \frac{-wr^4}{12\kappa} + c_1 r + c_2 \tag{9}$$

By applying the steady state B.Cs, as stated above, one can get the values of the constants c_1 and $c_2$and put in eq. (9) to get:

$$\Phi_s(r,t) = \frac{wr(R^3 - r^3)}{12\kappa} \tag{10}$$

The same B is needed to get a solution for a homogeneous equation. Cs will be applied by neglecting source term, i.e., $\frac{w}{\lambda} r^2$, equation (8) becomes:

$$\frac{1}{D}\frac{\partial \Phi_h}{\partial t} = \frac{\partial^2 \Phi_h}{\partial r^2} \tag{11}$$

with B.Cs

$$\Phi_h(0,t) = r\,(T(0,t) - T_0) = 0$$
$$\Phi_h(R,t) = R(T(R,t) - T_0) = 0$$
$$\Phi_h(r,0) = \frac{wr(R^3 - r^3)}{12\kappa} \tag{i}$$

For the solution of eq. (11), we use the separation of variables:

Let $\Phi_h(r,t) = R(r)\,T(t)$ $\tag{12}$

On differentiating the above equation concerning 'r' & 't', we arrive at $R''(r) + R(r)\lambda = 0$, $T'(t) + DT(t)\lambda = 0$, where $\lambda = \frac{R''(r)}{R(r)} = \frac{1}{D}\frac{T'(t)}{T(t)}$

$$R''(r) + \lambda R(r) = 0 \tag{13}$$
$$\text{And } T'(t) + D\lambda T(t) = 0 \tag{14}$$

Applying B.Cs

$$\Phi_h(0,t) = R(0)\,T(t) = 0$$
$$\Phi_h(R,t) = R(r)\,T(t) = 0$$

To above equations (9), we arrive at the solutions, i.e.,

$$R(r) = c\,sin\left(\frac{n\pi r}{R}\right) \tag{15}$$

with $R(0) = R(r) = 0$ for $T(t) \neq 0$. Similarly, solving for eq. (14) we get

$$T(t) = Ae^{-D\left(\frac{n\pi r}{R}\right)^2 t} \tag{16}$$

Putting back these eqs.(15) & (16) in eq. (12), and after simplification, we get:

$$\Phi_h(r,t) = \sum_{n=1}^{\infty} A_n sin\,(n\pi r/R)e^{-D(n\pi/R)^2 t} \tag{ii}$$

On comparing both the homogenous state eqs. (i) and (ii), we arrive at:

$$-\frac{wr(R^3 - r^3)}{12\kappa} = \sum_{n=1}^{\infty} A_n sin\,(n\pi r/R)e^{-D(n\pi/R)^2 t} \tag{17}$$

where is a constant $A_n = \frac{2}{R}\int F(x)sin(n\pi r/R)dr$ and $F(x) = -\frac{wr(R^3 - r^3)}{12\kappa}$. Substituting the value of $F(x)$ and integrating eq. (17) by parts, we get:

$$A_n = \underbrace{\frac{-wR^2}{6\kappa}\int_0^R rsin\left(\frac{n\pi r}{R}\right)dr}_{\textbf{I}_1} + \underbrace{\frac{w}{6R\kappa}\int_0^R r^4 sin\left(\frac{n\pi r}{R}\right)dr}_{\textbf{I}_2} \tag{18}$$

$I_1 = \frac{-wR^2}{6\kappa}\int_0^R rsin\left(\frac{n\pi r}{R}\right)dr$ and $I_2 = \frac{w}{6R\kappa}\int_0^R r^4 sin\left(\frac{n\pi r}{R}\right)dr$. After simple integration, we arrive at the solutions, i.e. $I_1 = \frac{wR^4}{6\kappa}\frac{(-1)^n}{n\pi}$ and $I_2 = \frac{w}{6R\kappa}[\frac{-R^5(-1)^n}{n\pi} - \frac{12R^5(-1)^n}{(n\pi)^3} + \frac{24R^5(-1)^n}{(n\pi)^5}\{(-1)^n - 1\}]$. By putting values of I_1 and I_2 in eq. (18) to get the value of A_n:

$$A_n = \frac{2wR^4}{\kappa}\frac{(-1)^n}{(n\pi)^3}[1 + \frac{2}{(n\pi)^2}\{(-1)^n - 1\}] \tag{19}$$

Now put back the value of A_n into eq. (ii) we get

41

$$\Phi_h(r,t) = \sum_{n=1}^{\infty} \frac{2wR^4}{\kappa} \frac{(-1)^n}{(n\pi)^3} [1 + \frac{2}{(n\pi)^2} \{(-1)^n - 1\}] sin\left(\frac{n\pi r}{R}\right) e^{-D\left(\frac{n\pi}{R}\right)^2 t} \tag{20}$$

The final solution for $\Phi(r,t)$ can be obtained by combining thesteady state solution and the homogeneous solution in the form,

$$\Phi(r,t) = \Phi_s(r,t) + \Phi_h(r,t)$$
$$\Phi(r,t) = \frac{wr(R^3-r^3)}{12\kappa} + \sum_{n=1}^{\infty} \frac{2wR^4(-1)^n}{(n\pi)^3}\left[1 + \frac{2}{(n\pi)^2}\{(-1)^n - 1\}\right] sinc\left(\frac{n\pi r}{R}\right)$$
$$e^{-D\left(\frac{n\pi}{R}\right)^2 t} \tag{21}$$

On reverse transformation, $\Phi T \longrightarrow$

$$\Phi(r,t) = r(T(r,t) - T_0)$$

We arrive at our final solution:

$$T(r,t) = T_0 + \frac{w(R^3-r^3)}{12\kappa} + \sum_{n=1}^{\infty} \frac{2wR^3(-1)^n}{(n\pi)^3}\left[1 + \frac{2}{(n\pi)^2}\{(-1)^n - 1\}\right]$$
$$sinc\left(\frac{n\pi r}{R}\right) e^{-D\left(\frac{n\pi}{R}\right)^2 t} \tag{22}$$

As time endures, the temperature of the whole tumor will reach the steady state where we can measure the final temperature of the tumor - the steady state temperature. The effect of heat diffusion within the tumor and in the surrounding healthy tissues can also be investigated by modeling more realistic assumptions in the model.

Temperature across the tumor will almost reach steady as time collapses. At this point, we can measure the final temperature of the tumor (denoted by T_s). From that steady state temperature and original temperature (T_0) of the tumor, we can determine the thermal conductivity of the tumor by using the relationship deduced from the solution (18) as given below in eq. (23). This can be further used to stimulate the more realistic heat diffusion from the tumor to nearby surrounding tissues in an advanced model. When the temperature of the tumor reaches to steady state. i.e., at *r = 0.* Eq. (22) becomes:

$$T_s = T_0 + \frac{wR^3}{12\kappa} \tag{23}$$

Table 5
Thermal conductivity, specific heat capacity, density, and thermal diffusivity of healthy and tumorous lung tissue (Giering, Lamprecht, Minet, & Handke, 1995)

Material	κ (W m^{-1} K^{-1})	c (J g^{-1} K^{-1})	ρ (Kg m^{-3})	D (m^2.s^{-1})
Lung Tissue	0.11	4.2	161	$1.62*10^{-7}$
Tumorous Lung Tissue	0.552	4.17	998	$1.32*10^{-7}$

Where the parameters, such as thermal conductivity (κ), specific heat capacity (c), density (ρ), and thermal diffusivity (D) of healthy and tumorous lung tissue, are taken from the literature (Giering et al., 1995).

From Fig. 8, one can see the temperature dependence on the radius of the human lung tumor. This figure shows that temperature is nearly constant for almost 1 cm of the radius. Then it starts decreasing onward and drops off to human body temperature at the peripheries, i.e., 4 cm. This is because of the imposed conditions over the problem. It is pertinent to mention that the temperature is obtained in the therapeutic range (42 – 48 oC) for cancer treatment of lung tumors. Without imposing such conditions on the problem, heat would have been propagated out of the tumor. This figure does not show a realistic situation. To combat the realistic situation, one cantackle this problem with advanced modeling techniques, for instance, with an approach using the finite difference method.
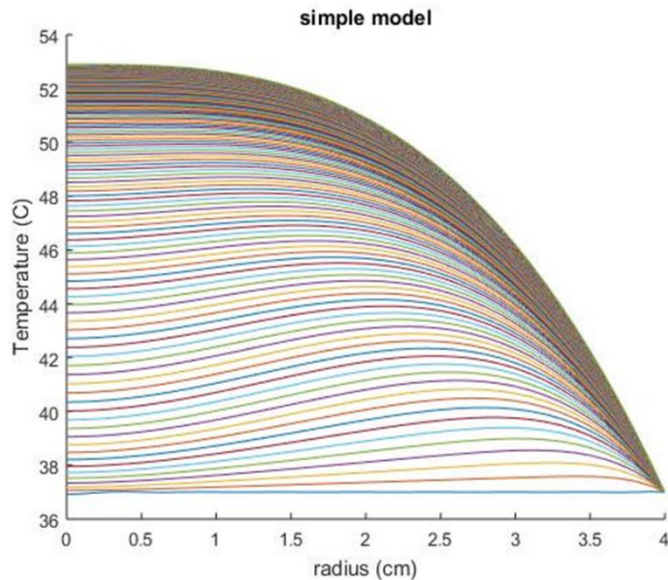
Figure 8: Temperature as a function of the radius of the tumor. Every individual line represents a specific time point

Figure 9 shows the temperature produced by the prepared nanoparticles, i.e., $NiFe_2O_4$, as a function of the radius of the human lung's tissue and time to get the maximum temperature in the therapeutic range. Here, we see that temperature increases as time passes and reaches its maximum value (52.5 ℃) and then starts decreasing from the center to the peripheries of the lung's tumor with the assumed radius size of 4 cm.
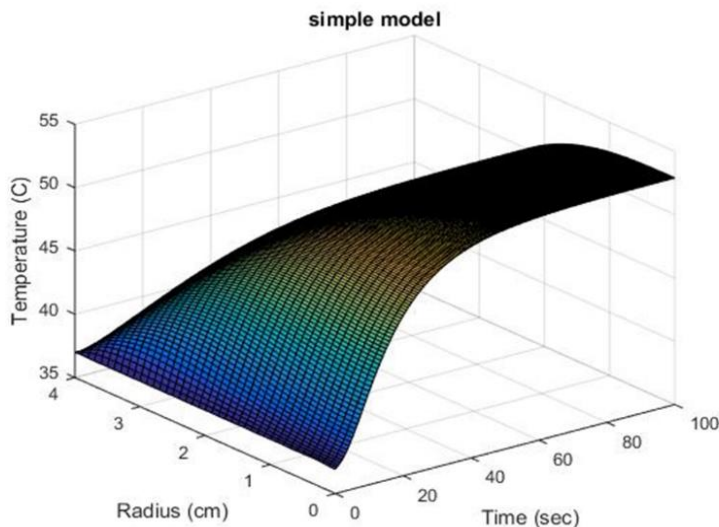

Figure 9: Temperature as a function of time and distance from the center of the tumor obtained from the analytical solution of the problem

Conclusions

The $NiFe_2O_4$ MNPs with crystallite sizes in the 15 – 55 nm range were prepared via the co-precipitation route. The samples showed ferromagnetic behavior, and a decrease in saturation magnetization with the temperature rise was observed for samples S4 and S5.However, sample S5 was found to have large saturation magnetization at all temperatures compared to the sample S4. The coercivity of sample S4 was larger than that of S5; however, the coercivity and magnetization (Zeeman energy) for both samples are nearly the same, suggestingalmost the same heating capabilities for these samples. From hyperthermia measurements, sample S4 was found to be the most suitable candidate for hyperthermia applications at 543 kHz because of its ability to produce heat in the therapeutic range of 42 – 48 ℃ and having a high*SAR* value. We found from the heat

diffusion equation modeling that temperature reaches a maximum constant value of 52.5 ℃ within 2 minutes and then drops when moving towards the lung's tumor peripheries. Although the modeling results are not that realistic in the current study, they can be made realistic in a more advanced and suitable modeling using the same heat diffusion equation from the perspective of hyperthermia treatment of cancer.

Reference

Bae, S., Lee, S. W., & Takemura, Y. (2006). Applications of NiFe2O4 nanoparticles for a hyperthermia agent in biomedicine. *Applied Physics Letters, 89*(25).

Bañobre-López, M., Teijeiro, A., & Rivas, J. (2013). Magnetic nanoparticle-based hyperthermia for cancer treatment. *Reports of Practical Oncology & Radiotherapy, 18*(6), 397-400.

Cihoric, N., Tsikkinis, A., van Rhoon, G., Crezee, H., Aebersold, D. M., Bodis, S., . . . Wust, P. (2015). Hyperthermia-related clinical trials on cancer treatment within the ClinicalTrials. gov registry. *International journal of hyperthermia, 31*(6), 609-614.

Dennis, C., Jackson, A., Borchers, J., Ivkov, R., Foreman, A., Hoopes, P., . . . Lau, J. (2008). The influence of magnetic and physiological behaviour on the effectiveness of iron oxide nanoparticles for hyperthermia. *Journal of Physics D: Applied Physics, 41*(13), 134020.

Giering, K., Lamprecht, I., Minet, O., & Handke, A. (1995). Determination of the specific heat capacity of healthy and tumorous human tissue. *Thermochimica acta, 251*, 199-205.

Hildebrandt, B., Wust, P., Ahlers, O., Dieing, A., Sreenivasa, G., Kerner, T., . . . Riess, H. (2002). The cellular and molecular basis of hyperthermia. *Critical reviews in oncology/hematology, 43*(1), 33-56.

Hussain, Y., Islam, L., Khan, H., Filosa, R., Aschner, M., & Javed, S. (2021). Curcumin–cisplatin chemotherapy: A novel strategy in promoting chemotherapy efficacy and reducing side effects. *Phytotherapy Research, 35*(12), 6514-6529.

Kakehi, M., Ueda, K., Mukojima, T., Hiraoka, M., Seto, O., Akanuma, A., & Nakatsugawa, S. (1990). Multi-institutional clinical studies on hyperthermia combined with radiotherapy or chemotherapy in advanced cancer of deep-seated organs. *International journal of hyperthermia, 6*(4), 719-740.

Kalambur, V. S., Han, B., Hammer, B. E., Shield, T. W., & Bischof, J. C. (2005). In vitro characterization of movement, heating and visualization of magnetic nanoparticles for biomedical applications. *Nanotechnology, 16*(8), 1221.

Kumar, C. S., & Mohammad, F. (2011). Magnetic nanomaterials for hyperthermia-based therapy and controlled drug delivery. *Advanced drug delivery reviews, 63*(9), 789-808.

Kuwano, H., Sumiyoshi, K., Watanabe, M., Sadanaga, N., Nozoe, T., Yasuda, M., & Sugimachi, K. (1995). Preoperative hyperthermia combined with chemotherapy and irradiation for the treatment of patients with esophageal carcinoma. *Tumori Journal, 81*(1), 18-22.

Menelaou, M., Georgoula, K., Simeonidis, K., & Dendrinou-Samara, C. (2014). Evaluation of nickel ferrite nanoparticles coated with oleylamine by NMR relaxation measurements and magnetic hyperthermia. *Dalton Transactions, 43*(9), 3626-3636.

Pradhan, P., Giri, J., Banerjee, R., Bellare, J., & Bahadur, D. (2007). Preparation and characterization of manganese ferrite-based magnetic liposomes for hyperthermia treatment of cancer. *Journal of Magnetism and Magnetic Materials, 311*(1), 208-215.

Šepelák, V., Bergmann, I., Feldhoff, A., Heitjans, P., Krumeich, F., Menzel, D., . . . Becker, K. D. (2007). Nanocrystalline nickel ferrite, NiFe2O4: mechanosynthesis, nonequilibrium cation distribution, canted spin arrangement, and magnetic behavior. *The Journal of Physical Chemistry C, 111*(13), 5026-5033.

Singh, B. (1990). Hyperthermia--a new dimension in cancer treatment. *Indian journal of biochemistry & biophysics, 27*(4), 195-201.

Stefanou, G., Sakellari, D., Simeonidis, K., Kalabaliki, T., Angelakeris, M., Dendrinou-Samara, C., & Kalogirou, O. (2014). Tunable AC magnetic hyperthermia efficiency of Ni ferrite nanoparticles. *IEEE transactions on magnetics, 50*(12), 1-7.

Szasz, O., Szigeti, G. P., Szasz, A., & Benyo, Z. (2018). Role of electrical forces in angiogenesis. *Open Journal of Biophysics, 8*(02), 49.

Tazikeh, S., Akbari, A., Talebi, A., & Talebi, E. (2014). Synthesis and characterization of tin oxide nanoparticles via the Co-precipitation method. *Materials Science-Poland, 32*, 98-101.

Tomitaka, A., & Takemura, Y. (2019). Magnetic Relaxation of Intracellular Magnetic Nanoparticles for Hyperthermia. *Critical Reviews™ in Biomedical Engineering, 47*(6).

Westermark, F. (1898). Uber die Behandlung des ulcerirenden Cervix carcinoma mittels Knonstanter Warme. *Zentralbl Gynkol*, 1335-1339.